Earth and Planetary Science Letters 493 (2018) 118–127

Contents lists available at ScienceDirect

Earth and Planetary Science Letters

www.elsevier.com/locate/epsl

The elastic properties of *hcp*-Fe alloys under the conditions of the Earth's inner core

Yunguo Li[a,*], Lidunka Vočadlo[a], John P. Brodholt[a,b]

[a] Department of Earth Sciences, University College London, Gower Street, London WC1E 6BT, United Kingdom
[b] Centre for Earth Evolution and Dynamics (CEED), University of Oslo, 0316 Oslo, Norway

ARTICLE INFO

Article history:
Received 25 November 2017
Received in revised form 27 February 2018
Accepted 9 April 2018
Available online 25 April 2018
Editor: B. Buffett

Keywords:
Earth's inner core
AIMD
elasticity
iron alloys

ABSTRACT

Geophysical and cosmochemical constraints suggest the inner-core is mainly composed of iron with a few percent of light elements. However, despite extensive studies over many years, no single alloying light-element has been found that is able to simultaneously match the observed inner-core density and both seismic velocities. This has motivated a number of suggestions of other mechanism to lower velocities, such as anelasticity or premelting. However, an unexplored possibility is that a combination of two or more light-elements might produce the desired reduction in velocities and densities of the inner core. In order to test this, we use *ab initio* molecular dynamics calculations to map the elastic property space of *hcp*-Fe alloyed with S, Si and C at 360 GPa up to the melting temperature. Based on a mixing solid solution model together with direct simulations on the ternaries, we found a number of compositions which are able to match the observed properties of the inner core. This is the first time that the density, V_P, V_s and the Poisson's ratio of the inner core have been matched directly with an *hcp*-Fe alloy.

1. Introduction

The Earth has a solid inner core which is predominantly made of iron (Fe) and ∼5 wt.% nickel (Ni), together with some light elements to account for the core density deficit (Hillgren et al., 2000). As well as being too dense, pure iron (either *hcp* or *bcc*) also has seismic velocities at inner-core conditions that are higher (10–30%) than those obtained by seismology (e.g. Litasov and Shatskiy, 2016), requiring that both density and velocity must be reduced by either light elements, or by some other mechanism. Many attempts have been made to estimate the effect of light elements on velocities and/or densities, including S, Si, C, O and H (Antonangeli et al., 2010; Bazhanova et al., 2012; Belonoshko et al., 2007; Caracas, 2015; Hirose et al., 2017; Martorell et al., 2013b; Sakamaki et al., 2016; Tagawa et al., 2016; Vočadlo, 2007), but while these Fe-alloys can match some properties of the inner core (i.e. density or velocity) none of them can match both P- and S-velocities and the density of the inner core simultaneously. Indeed, all the iron compounds examined so far except hexagonal Fe_7C_3 (Bazhanova et al., 2012; Chen et al., 2014; Prescher et al., 2015), show higher velocities than the core up to their melting temperatures, but Fe_7C_3 has too low a density (Li et al., 2016).

Recent computer simulations revealed that pure *hcp*-Fe could match the observed sound wave velocities as a result of premelting softening (Martorell et al., 2013b), but the calculated densities were still too high even at temperatures up to its melting point (Martorell et al., 2013b) and so a light element is still required. However, alloying iron with light elements in some cases suppresses the premelting softening and consequently increases the seismic velocities (Martorell et al., 2016).

One thing that has not been properly addressed so far is whether a combination of elements is able to produce the required velocities and densities of the inner core. This is a natural thing to try, especially since it is becoming clear that more than one element is needed to reproduce the properties of the outer core (Antonangeli et al., 2010; Badro et al., 2014; Bazhanova et al., 2017; Brodholt and Badro, 2017; Morard et al., 2014). We therefore performed *ab initio* molecular dynamics (AIMD) to study the thermoelasticity of *hcp*-Fe alloyed with Si, S and C under inner-core conditions (360 GPa). Ni can be safely ignored considering its negligible effects on the elastic properties of Fe at core temperatures (Martorell et al., 2013a). We have not considered oxygen since most oxygen preferentially partitions into the outer core (Alfè et al., 2002). There is of course a possibility that a mixture of *hcp*-Fe and a distinct FeO phase might provide a pathway for oxygen into the inner core, but that is beyond the scope of this paper. We have also not yet included the effect of other light elements such as H. Although Umemoto and Hirose (2015) found that the density and

---

* Corresponding author.
E-mail address: yunguo.li@ucl.ac.uk (Y. Li).

https://doi.org/10.1016/j.epsl.2018.04.013

V_p of liquid Fe with about 1 wt% H can match those the outer core, the evidence so far for the inner core is less positive. Indeed, Caracas (2015) found the H actually increased V_s of *hcp*-Fe, the opposite of what it required. Nevertheless, the velocities of H-bearing *hcp*-Fe should be considered in the future.

In this work, we aim to map the elastic property space of *hcp*-Fe alloys under inner-core conditions in the iron-rich corner. We first calculate the elasticity of the three binary systems (*hcp*-Fe–C, *hcp*-Fe–S and *hcp*-Fe–Si) under inner core conditions. We then extend this to the three ternary systems (*hcp*-Fe–Si–C, *hcp*-Fe–Si–S, and *hcp*-Fe–S–C) and use the elastic properties of the binaries to fit to a multicomponent mixing model. Using this model, we search for all possible compositions which are able to reproduce the density and the P- and S-velocities of the inner core. We find, for the first time, a number of alloys which match both the density and seismic velocities with the preliminary reference Earth model (PREM) before melting.

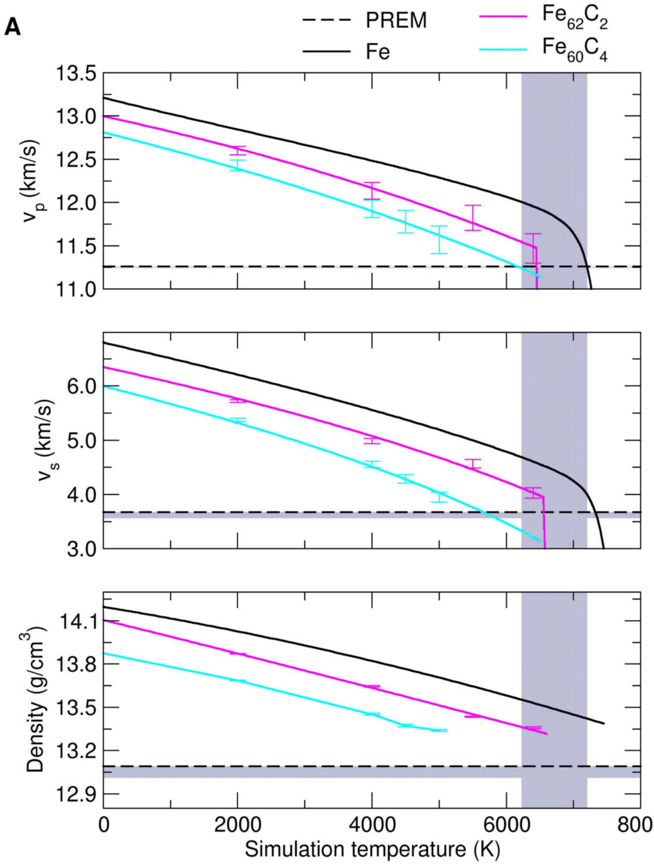

Fig. 1. Calculated ρ, V_s and V_p at 360 GPa as a function of temperature of (**A**) *hcp*-$Fe_{62}C_2$ and *hcp*-$Fe_{60}C_4$, (**B**) *hcp*-$Fe_{60}Si_4$ and *hcp*-$Fe_{56}Si_8$, and (**C**) *hcp*-$Fe_{62}S_2$ and *hcp*-$Fe_{60}S_4$ compared with those of *hcp*-Fe (Martorell et al., 2013b) and PREM. The curves of density are guides to the eye. The curves of sound velocities, except for the *hcp*-$Fe_{60}C_4$, are fits to the Nadal–Le Poac (NP) model (Nadal and Le Poac, 2003). The dashed lines with a shaded region indicate the PREM data, and the other shaded regions indicate the possible temperatures at ICB.

2. Methods

2.1. *Ab initio calculations*

We performed calculations using DFT with the same technical parameters used in (Martorell et al., 2013b). We used a simulation box of the same size (64 atoms) to the calculation of *hcp*-Fe, VASP code (Kresse and Joubert, 1999), PAW potentials (Kresse and Furthmüller, 1996) (with valence configurations Ar-$3d^6 4s^2$, Ne-$3s^2 3p^2$, Ne-$3s^2 3p^2$ and He-$2s^2 2p^2$ for Fe, Si, S and C, respectively), and a plane wave cut-off of 400 eV. Exchange-correlation effects were treated in the generalized gradient approximation (GGA) with the Perdew–Wang scheme (Perdew and Wang, 1992). Single particle orbitals were populated according to the Fermi–Dirac statistics.

We ran finite temperature Born–Oppenheimer AIMD to derive the equilibrium structure and calculate properties. The integration (with the time step of 1.0 fs) of the classical Newton's equations of motion uses the Verlet algorithm, and the ground-state search is done within an efficient iterative matrix diagonalization scheme and a Pulay mixer for each step.

Simulations were first performed at targeted temperatures using an Andersen thermostat, with a restarting value of no less than 200 cycles. Then we ran VASP-NPT simulations for the isothermal-isobaric ensemble, using the barostat implemented in VASP by Hernández (2001), to relax the unit-cell parameters at the targeted temperatures and pressures; these simulations were run for over 10 ps, which is enough to reach reasonable convergence. The lattice parameters averaged (based on the last 9 ps) from these NPT simulations were then used to create unit cells to which distortions were applied (see Section 2.2). We retrieved the root-mean-square displacements (RMSD) and averaged coordination numbers for each simulation to ensure that we were computing the solid phases.

Badro et al. (2014) found that a small pressure correction was needed in order to correct for the slight difference in GGA density with that obtained from shock experiments. At 350 GPa, the pressure correction is ~8 GPa, which for a bulk modulus of 1435 GPa, would change the density by less than 0.5%, and the effect on velocities would be even smaller. We have, therefore, not applied a pressure correction as our results presented later (Fig. 1) show that this error is much less than the misfit to the core for all binary alloys (see Fig. 1), and for the ternaries is outweighed by uncertainties in the core temperatures (Fig. 4).

2.2. *Elastic properties calculations*

We used the strain–stress method to calculate the isothermal elastic constants. Adiabatic elastic constants can also be calculated either directly by the strain-energy method or from the isothermal elastic constants via thermodynamic equations (Oganov et al., 2001; Wallace, 1998), but since high P/T experiments only measure aggregated properties, we can first calculate the isothermal elastic constants and convert the isothermal aggregated properties to adiabatic aggregated properties. The lattice parameters obtained from NPT simulations were used to create strained unit cells. Two distortion matrices were applied to the relaxed equilibrium structures:

$$\begin{pmatrix} 1+\delta & 0 & 0 \\ 0 & 1 & \delta/2 \\ 0 & \delta/2 & 1 \end{pmatrix} \quad \text{and} \quad \begin{pmatrix} 1 & 0 & 0 \\ 0 & 1 & 0 \\ 0 & 0 & 1+\delta \end{pmatrix}$$

The stresses on the strained simulation boxes were then obtained from NVT simulations run over 10 ps. The isothermal elastic moduli c_{ij} (Simmons et al., 1971) were evaluated using the stress–strain method by the standard relation $\sigma_{ij} = c_{ijkl} \cdot \varepsilon_{kl}$. Four different strains (±0.01 and ±0.02) were applied in each distortion and the resulting stress–strain values were then fitted to second-order polynomials; by evaluating the slopes at zero strain, the stress–strain relationship in the limit of equilibrium volume is then determined (Karki et al., 2001). The calculated isothermal elastic constants and aggregated properties are shown in Table S1. The adiabatic elastic constants were also calculated from the isothermal elastic constants and tabulated in Table S2.

Since we apply an uniform strain to the supercell, it is natural to use the Voigt average (Simmons et al., 1971) to evaluate the ag-

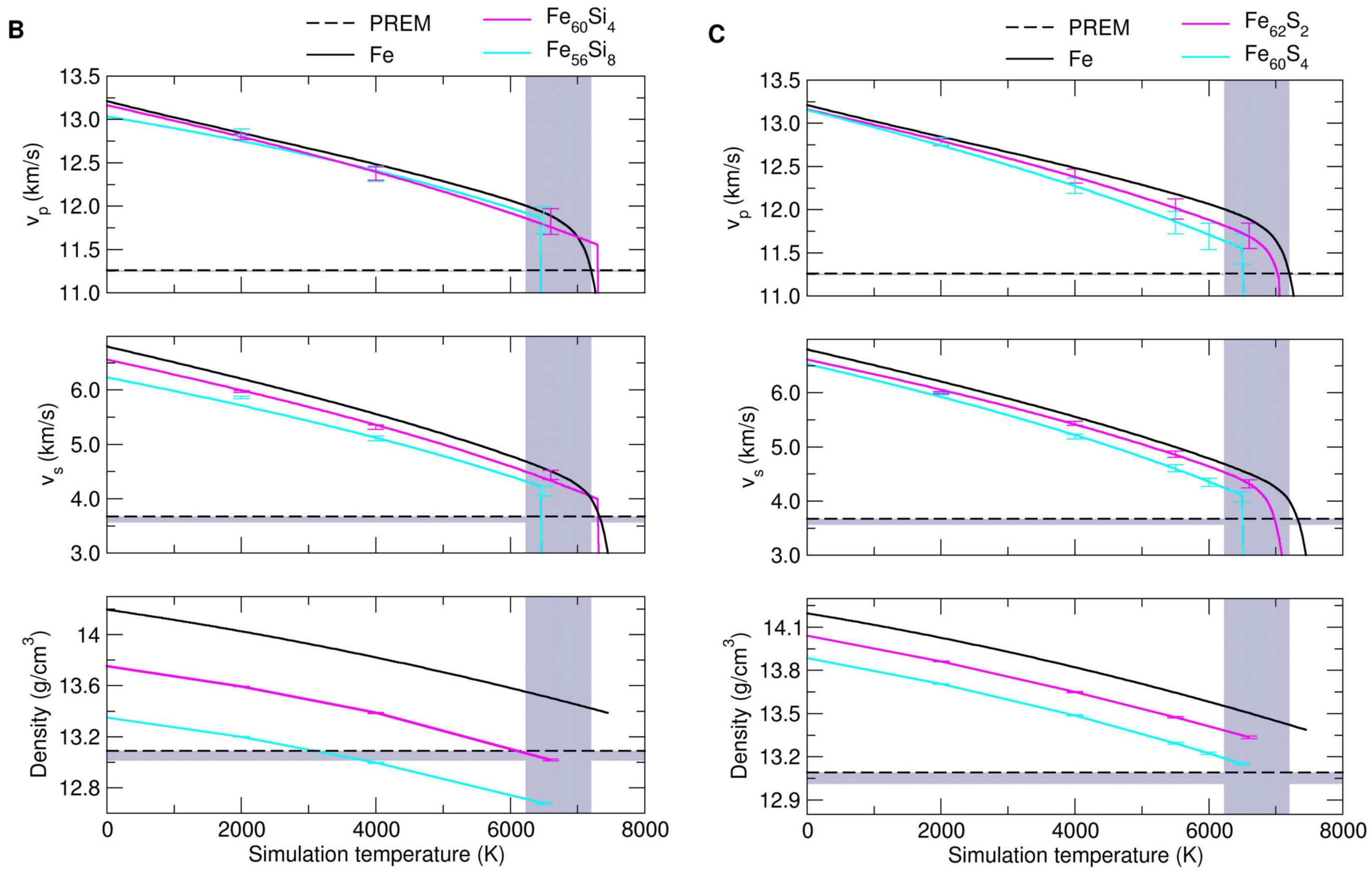

Fig. 1. (*continued*)

gregated elastic properties. The Voigt average is also more robust at high pressures (Crosson and Lin, 1971), which calculates the incompressibility (B_T) and shear modulus (G) by

$$B_T = [2(c_{11} + c_{12}) + 4c_{13} + c_{33}]/9 \tag{1}$$

$$G = (12c_{44} + 7c_{11} - 5c_{12} + 2c_{33} - 4c_{13})/30 \tag{2}$$

The adiabatic incompressibility, B_S is obtained from

$$B_S = B_T(1 + \alpha\gamma T) \tag{3}$$

where α is the volumetric thermal expansion coefficient (1×10^{-5}/K) (Vočadlo, 2007; Vočadlo et al., 2003), B_T is the isothermal bulk modulus, γ is the Grüneisen parameter, and $\gamma = 1.5$ (Vočadlo, 2007; Vočadlo et al., 2003).

The isotropic wave propagation velocities in the material can then be evaluated from the elastic moduli and the density, ρ, as follows:

$$V_p = \sqrt{\frac{B_s + \frac{4}{3}G}{\rho}} \tag{4}$$

and

$$V_s = \sqrt{\frac{G}{\rho}} \tag{5}$$

The Debye sound velocity V_D has the relationship with V_p and V_s:

$$\frac{3}{V_D^3} = \frac{1}{V_p^3} + \frac{2}{V_s^3} \tag{6}$$

The Poisson's ratio is obtained by

$$\nu = \frac{3B_s - 2G}{6B_s + 2G} \tag{7}$$

2.3. NP shear modulus model

The Nadal–Le Poac (NP) shear modulus model (Nadal and Le Poac, 2003) based on Lindemann melting theory, was employed to depict the temperature dependence of G at a fixed pressure. The NP model is:

$$G(P,T) = \frac{1}{J(T)}\left[\left(G_0 + \frac{\partial G}{\partial P}\frac{P}{\sqrt[3]{\eta}}\right)\left(1 - \frac{T}{T_m}\right) + \frac{\rho}{Cm}k_b T\right] \tag{8}$$

where

$$C = \frac{(6\pi)^{(\frac{2}{3})}}{3} f^2 \tag{9}$$

$$J(T) = 1 + \exp\left[-\frac{1 + \frac{1}{\zeta}}{1 + \frac{\zeta}{1 - \frac{T}{T_m}}}\right] \tag{10}$$

and

$$G_P = G_0 + \frac{\partial G}{\partial P}\frac{P}{\sqrt[3]{\eta}} \tag{11}$$

In Eqs. (8)–(11), G is the shear modulus, G_0 is the shear modulus at 0 K and 0 GPa, P is pressure, T is temperature, T_m is the melting temperature, ρ is the density, m is the averaged atomic mass, η is the compression defined as the ratio of the density at current conditions to the density at 0 K and 0 GPa, k_b is the Boltzmann constant, f is the Lindemann constant for the material and ζ is a material parameter. Our results were fitted to this NP model with four adjustable parameters, namely, T_m, G_P, C and ζ (G_P was taken as a constant as explained in point Martorell et al., 2013b).

2.4. Error analysis

The statistical errors of the temperatures and stresses were evaluated by the blocking method for correlated data (Flyvbjerg and Petersen, 1989). The standard deviation is defined as:

$$\delta = \sqrt{\frac{c'_0}{n'-1}\left(1+\frac{1}{\sqrt{2(n'-1)}}\right)} \tag{12}$$

where $n' = n/2$, $c'_0 = \frac{1}{n'}\sum_{k=1}^{n'}(x'_k - \overline{x})^2$ and $x'_i = (x_{2i-1} + x_{2i})/2$; $\overline{x}$ is the average, n is the number of data points, n' is created to fragment the data points.

The final statistical error of the temperature increases from 3 to 15 K as the temperature increases from 0 to 7350 K; this represents in all cases an error of less than 0.5%. The final temperatures were averaged from the last 9 ps of the NPT simulations.

The statistical errors of the elastic constants were derived from the statistical errors of stresses, and hence the statistical errors of the aggregated elastic properties were also derived following the rule of error propagation:

$$\Delta F = \sqrt{\sum_A \left(\frac{\partial F}{\partial A}\right)^2 \Delta A^2} \tag{13}$$

where ΔF is the error of the aggregated property and ΔA is the error of the calculated property.

The statistical errors of the calculated elastic properties are listed in Table S3.

2.5. Ordered structures

The substitutional solid solution atoms were placed in the supercell symmetrically and evenly. We considered 10 separate configurations for the $Fe_{62}A_2$ alloys, 10 for the $Fe_{60}A_4$ alloys, 6 for the $Fe_{60}A_3B_1$ alloys, and 15 for the $Fe_{60}A_2B_2$ alloys (A and B indicate the solid solutes). Only the most energetically stable configurations were used for elastic calculations. The short-range order (SRO) can be measured by the Warren–Cowley parameter, which is defined as $\alpha = 1 - P_B(R)/m_B$ (where $P_B(R)$ is the probability of finding a B atom at a distance R from an A atom and m_B stands for the molar fraction of B) for a binary $A_{1-m}B_m$ alloy. The Warren–Cowley parameter characterizes the clustering and SRO by $\alpha > 0$ and $\alpha < 0$, respectively. Our selected structures exhibit SRO.

2.6. Disordered structures

It should be pointed out that only the disordered structures are relevant to the Earth's core, though the ordered structures are also useful. However, the uncertainties that result from using an ordered model should explored. The randomness of alloy structures can be described by a 'lattice algebra'. Each atomic site can be assigned with a spin variable σ_i ($\sigma_i = \pm 1$ for binary alloys, and $\sigma_i = \pm 1$ or 0 for ternary alloys). A group of k lattice sites spanning a maximum distance of m (m indicates the mth nearest neighbor distance) are defined as a graph $f = (k, m)$. Then, a multisite correlation function $\overline{\Pi}_{k,m}$ that can be established by taking the product of σ_i over all sites within a graph and averaging over all symmetry-degenerate graphs will perfectly characterize the randomness of alloy structures. To achieve the maximum randomness within a supercell as small as possible, Zunger et al. (1990) developed the special quasi-random structure (SQS) approach, which strives to find small-unit-cell structures that possess the multisite correlation functions $(\overline{\Pi}_{k,m})_{SQS} \cong (\overline{\Pi}_{k,m})_{random}$ for as many clusters as possible. We have generated SQSs for the binary *hcp*-$Fe_{60}Si_4$ and the ternary *hcp*-$Fe_{60}Si_2C_2$ alloys using the mcsqs (Monte Carlo algorithm for SQS searching) code (van de Walle et al., 2013) in ATAT (Alloy Theoretic Automated Toolkit). The generated SQS structures are shown in Fig. S1. All correlations of the SQSs requested can match the random alloys within satisfactory errors, as can be seen in Fig. S1.

The calculated elastic constants of the SQSs of the binary *hcp*-$Fe_{60}Si_4$ and the ternary *hcp*-$Fe_{60}Si_2C_2$ alloys are shown in Table S1 and Fig. S1, in comparison with those of ordered structures. For the binary *hcp*-$Fe_{60}Si_4$, the difference of density between the SQS and ordered structure is less than 1% up to the melting. The difference in elastic constants is larger and up to 6%. However, the aggregated elastic properties (B_s, G, V_s and V_p) of the SQS and ordered structures match within the statistical errors. For the ternary *hcp*-$Fe_{60}Si_2C_2$, the differences of elastic constants between the SQS and the ordered structure is smaller than the binary. The densities of the SQS and the ordered structure are almost indistinguishable. The bulk modulus, shear modulus, and sound velocities of the SQS structure match those of the ordered structure at all temperatures within the statistical error.

2.7. Break of symmetry

The addition of light elements in *hcp*-Fe breaches the hexagonal lattice symmetry. The deviation of symmetry is very weak for the ordered structures, and it is safe to calculate the elastic constants following the hexagonal symmetry. However, this deviation is stronger in the SQS structures. The inter-axial angles of the ternary *hcp*-$Fe_{60}Si_2C_2$ SQS structure at 6500 K are 90.16°, 89.960°, and 119.80° for α, β, and γ, respectively. This structure has the strongest deviation of symmetry among the examined structures.

To evaluate the error in calculating elastic constants directly following hexagonal symmetry, we first calculated the elastic tensor of the ternary *hcp*-$Fe_{60}Si_2C_2$ SQS structure at 6500 K with full triclinic symmetry. We then projected the triclinic elastic tensor onto the hexagonal tensor, and compared that with the tensor directly calculated with hexagonal symmetry.

The calculated elastic tensor of the ternary *hcp*-$Fe_{60}Si_2C_2$ SQS structure at 6500 K following the triclinic symmetry is:

$$\begin{pmatrix} 1640 & 1344 & 1055 & -40 & 2 & 10 \\ 1344 & 1618 & 1079 & 16 & -52 & -44 \\ 1055 & 1079 & 1811 & 71 & 53 & 16 \\ -41 & 16 & 71 & 174 & 35 & 61 \\ 2 & -52 & 53 & 35 & 117 & 31 \\ 10 & -44 & 16 & 61 & 31 & 79 \end{pmatrix}$$

for which the standard deviation is:

$$\begin{pmatrix} 28 & 30 & 26 & 21 & 22 & 24 \\ 30 & 30 & 26 & 22 & 22 & 25 \\ 26 & 26 & 26 & 19 & 21 & 24 \\ 21 & 22 & 19 & 22 & 20 & 23 \\ 22 & 22 & 21 & 20 & 15 & 19 \\ 24 & 25 & 24 & 23 & 19 & 23 \end{pmatrix}$$

The triclinic tensor can be projected to the hexagonal tensor via $\boldsymbol{C}_{hexagonal} = \boldsymbol{P} \cdot \boldsymbol{C}_{triclinic}$, where $\boldsymbol{P}$ is the projector matrix defined by Moakher and Norris (2006). The derived elastic tensor $\boldsymbol{C}_{hexagonal}$ is:

$$\begin{pmatrix} 1578 & 1396 & 1067 & 0 & 0 & 0 \\ 1396 & 1578 & 1067 & 0 & 0 & 0 \\ 1067 & 1067 & 1811 & 0 & 0 & 0 \\ 0 & 0 & 0 & 146 & 0 & 0 \\ 0 & 0 & 0 & 0 & 146 & 0 \\ 0 & 0 & 0 & 0 & 0 & 182 \end{pmatrix}$$

Compared to the elastic constants directly calculated following the hexagonal symmetry (Table S1), the projected C_{11}, C_{12}, C_{13} and C_{33} differ by 2.0%, 2.6%, 4.7%, and 0.0%, respectively. The exception is C_{44} which differs by 16%, however, C_{44} is small compared to the other constants and does not contribute significantly to the aggregated properties. The derived bulk and shear modulus from the projected hexagonal elastic tensor are 1467 and 172 GPa, respectively, which are only 8 GPa and 6 GPa lower than those directly calculated following the hexagonal symmetry. Thus, the elastic calculation following the hexagonal symmetry leads to the overestimation of V_s and V_p by 3.4% and 0.8%, respectively.

3. Results and discussion

3.1. *Binary* hcp-*Fe alloys*

Our simulation starts with the *hcp*-Fe–C binary alloy. We considered two *hcp*-Fe–C alloys ($Fe_{62}C_2$ and $Fe_{60}C_4$), with the concentration of C up to 1.4 wt.%. Such concentrations include the compositional range proposed by Wood et al. (2013), who suggested a likely upper concentration of ~1 wt.% C in the core. We observed an immediate drop in both the density and bulk sound velocities upon the addition of C (Fig. 1A). For *hcp*-$Fe_{62}C_2$ (0.69 wt.% C), there is a 6.3% drop in the shear sound wave velocity (V_s) and a 2.0% drop in the compressive sound wave velocity (V_p) at 0 K, while, the density (ρ) dropped slightly by 0.6%. At 6500 K, V_s, V_p and ρ dropped by 15.8%, 3.5%, and 1.2%, respectively. The *hcp*-$Fe_{62}C_2$ alloy melted at 6600 K, which is significantly lower than that of pure iron obtained by similar methods (7350 K) (Martorell et al., 2013b). T_m can be further decreased by adding more C. We were only able to obtain the elastic constants of *hcp*-$Fe_{60}C_4$ up to 5000 K (the *hcp* lattice becomes unstable above 5000 K), and both the density and sound wave velocities also experienced a further decrease in comparison with the *hcp*-Fe and *hcp*-$Fe_{62}C_2$. However, the density of *hcp*-Fe–C alloys decreases at a slower rate than the sound velocities (as shown by the data of *h*cp-$Fe_{60}C_4$ at 5000 K). It can be inferred, therefore, that the sound velocities and density of *hcp*-Fe–C alloys cannot simultaneously match PREM and other light element candidates must be considered.

Si has been reported to significantly decrease the density of *hcp*-Fe under the inner-core conditions (Martorell et al., 2016). However, although the density decreases almost linearly with the increasing Si content, the sound velocities do not reduce sufficiently (Fig. 1B); therefore, pure *hcp*-Fe–Si binary must also be ruled out.

S has a similar chemical potential to Si in Fe, and it is believed to exist in the core owing to the widespread occurrence of iron sulfides in meteorites (Alfè et al., 2000). In addition, the solubility of S in Fe increases with increasing pressure and temperature (Kamada et al., 2012; Li et al., 2001). Thus, we considered two *hcp*-Fe–S alloys: $Fe_{62}S_2$ and $Fe_{60}S_4$. The density of *hcp*-Fe–S shows a continuous drop with the increasing concentration of S (Fig. 1C), and both V_s and V_p decrease. Compared to pure iron at 6500 K, the density dropped by 1.3% and 2.7%, V_s dropped by 5.3% and 12.0%, and V_p dropped by 0.9% and 2.5%, in $Fe_{62}S_2$ and $Fe_{60}S_4$, respectively. While the density matches within error (0.4%) the PREM density at 6500 K, V_s is higher than the PREM values by 11.1%. Again, this makes it impossible for the binary *hcp*-Fe–S alloy to simultaneously match both the PREM density and sound velocities.

The fact that both Fe–S and Fe–Si binary alloys cannot be the core material is consistent with the *ab initio* free energy calculations reporting that the density discontinuities at the inner-core boundary (ICB) cannot be matched by either of them alone (Alfè et al., 2000, 2002). Therefore, we can infer that there is no binary *hcp*-Fe alloy candidate for the inner core and the search for a suitable inner-core composition must go to high-order alloys or compounds. Consequently, we explored the thermoelastic properties of the following three ternary alloy systems, *hcp*-Fe–Si–C, *hcp*-Fe–S–C, and *hcp*-Fe–S–Si.

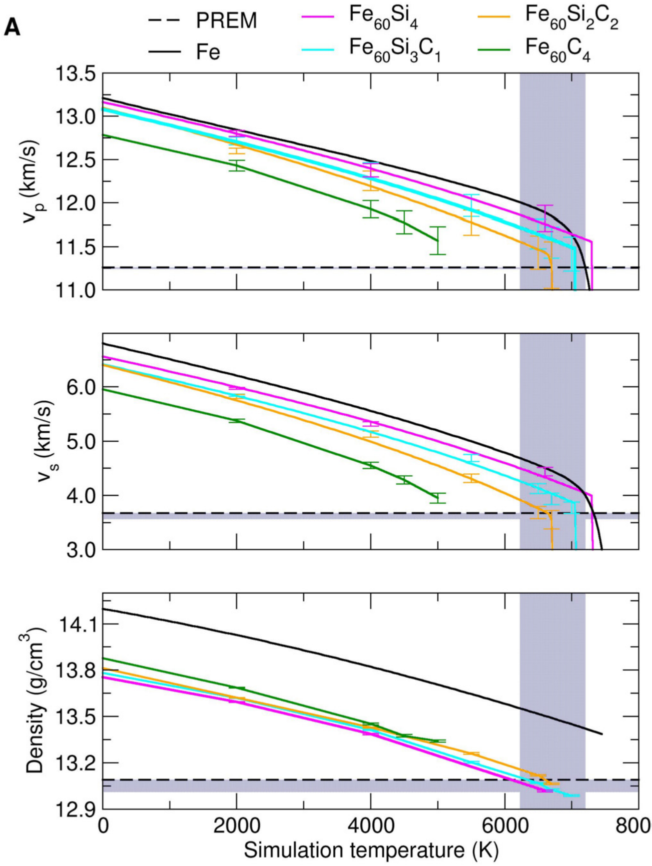

Fig. 2. Calculated ρ, V_s and V_p at 360 GPa as a function of temperature of (**A**) *hcp*-Fe–Si–C alloys, (**B**) *hcp*-Fe–S–Si alloys, and of (**C**) *hcp*-Fe–S–C alloys in comparison with the *hcp*-Fe (Martorell et al., 2013b), binary alloys and PREM. The curves of density are guides to the eye. The curves of sound velocities, except for the *hcp*-$Fe_{60}C_4$, are fits to the Nadal–Le Poac (NP) model (Nadal and Le Poac, 2003). The dashed lines with a shaded region indicate the PREM data, and the other shaded regions indicate the possible temperatures at ICB.

3.2. *Ternary* hcp-*Fe alloys*

We investigated the evolution in the elasticity of the *hcp*-Fe–Si–C system by studying two intermediate compositions between $Fe_{64}Si_4$ and $Fe_{60}C_4$, namely, the *hcp*-$Fe_{60}Si_3C_1$ and *hcp*-$Fe_{60}Si_2C_2$. The total molar fraction of light elements remains the same among these alloys, whereas only the Si/C ratio is allowed to vary. At 0 K, we observed an increase in density with the substitution of Si with C (Fig. 2A). Compared to *hcp*-$Fe_{60}Si_4$, V_s drops by 2.6% and 5.1% in *hcp*-$Fe_{60}Si_3C_1$ and *hcp*-$Fe_{60}Si_2C_2$, respectively, whereas V_p, drops by 0.8% and 1.6% respectively. At high temperatures, the elastic properties of *hcp*-$Fe_{60}Si_3C_1$ and *hcp*-$Fe_{60}Si_2C_2$ are in between those of *hcp*-$Fe_{60}Si_4$ and *hcp*-$Fe_{60}C_4$. Both *hcp*-$Fe_{60}Si_3C_1$ and *hcp*-$Fe_{60}Si_2C_2$ can match the density and sound wave velocities of PREM within statistical errors before melting, however, the match for the *hcp*-$Fe_{60}Si_3C_1$ occurs at a much higher temperature.

Although we find that *hcp*-$Fe_{60}Si_3C_1$ is able to match PREM density and seismic velocities close to the melting temperature ($T_m = 7100$ K), this is higher than most estimates of the

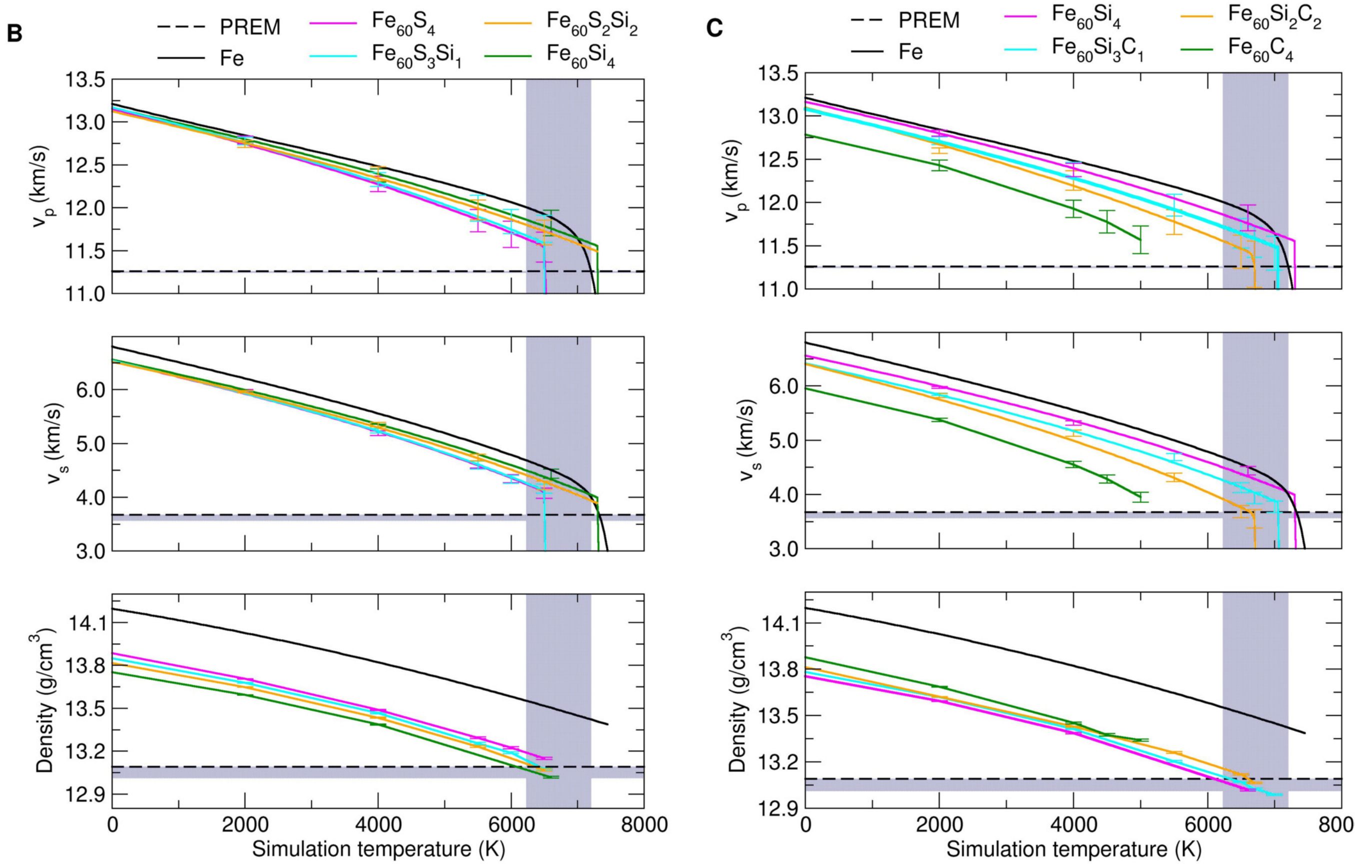

Fig. 2. (*continued*)

temperature of the inner core (Alfè, 2009). On the other hand, *hcp*-$Fe_{60}Si_2C_2$ matches the PREM density and seismic velocities at around 6500 K, a more reasonable inner core temperature. However, this is also close to its melting temperature which we find in our simulations ($T_m = 6700$ K). In general, these simulations overestimate the melting temperature since they do not contain defects or surfaces from which to nucleate melting. However, in this case we suggest that the overheating should be negligible since the atomic volume of C differs significantly to Fe, and has an equivalent effect on point defects. In other words, the melting temperature of *hcp*-$Fe_{60}Si_2C_2$ in our simulations should be close to the experimental one. Assuming this is the case, *hcp*-$Fe_{60}Si_2C_2$ can match the density and both seismic velocities of PREM before melting. Furthermore, the Poisson's ratio of *hcp*-$Fe_{60}Si_2C_2$ (Table S1) is in exact agreement with the observed value 0.44 of the inner core (Dziewonski and Anderson, 1981). The concentration of Si (1.6 wt.%) and C (0.7 wt.%) agree with other recent models for Si (1–2 wt.%) (e.g. Antonangeli et al., 2010) and C (0.1–0.7 wt.%) (e.g. Zhang and Yin, 2012). The concentration of Si also agrees with the compositional constraints of outer core (Badro et al., 2015, 2014) considering the partitioning (Alfè et al., 2002).

The density and the P- and S-velocities of *hcp*-$Fe_{60}Si_2C_2$ match the PREM values between 6500 and 6700 K. Although we used the ordered alloy structures, these exhibit almost identical elastic properties as the special quasi-random structure (SQS) (Zunger et al., 1990) of *hcp*-$Fe_{60}Si_2C_2$ (Table S1 and Fig. S1). In the ternary alloy, even the ordered structure has a lowered symmetry, reducing further the difference between the ordered and disordered structures.

None of the *hcp*-Fe–S–C and *hcp*-Fe–Si–S compositions we studied were able to match PREM densities and velocities. As discussed above, when adding Si or S, the core density is matched but the calculated sound velocities are still high compared to PREM. The mixture of Si and S in the *hcp*-Fe suffers the same problem (Fig. 2B). On the other hand, the *hcp*-Fe–S–C alloys studied all melted while its density was above that of PREM (Fig. 2C), This indicates that both S and C can induce a strong depression of the melting point and adding more S or C would further depress the melting temperature and reduce the density; but, even if the density could be matched, it would be at a temperature below 6000 K, considered likely to be too low for the inner core.

3.3. *Solid solution model*

So far, only *hcp*-$Fe_{60}Si_2C_2$ is able to match the properties of the core. However, we have been restricted to studying systems where the compositions are limited by the size of the simulated supercell. The question then is: are there other suitable compositions which we have not studied directly? In order to answer this, we fit our *ab initio* elastic constants calculated for the binary systems to a simple ideal solid solution model. This was done for three temperatures (5500, 6000, and 6500 K) and allows us to search for candidates in the whole compositional space.

The elastic constants at any composition can be obtained from a summation as a function of volume fraction (Chantel, 2014)

$$\psi_{ss} = \frac{1}{\sum_{i=1}^{n} \frac{1}{m_i V_i} \sum_{i=1}^{n} \frac{m_i V_i}{\psi_i}} \tag{14}$$

where ψ_{ss} is the bulk elastic property, n is the number of components in the alloy, m_i is the molar fraction of the component, and ψ_i and V_i are the partial molar elastic property and volume of a component i. In this case we just fit B_s and G, not the indi-

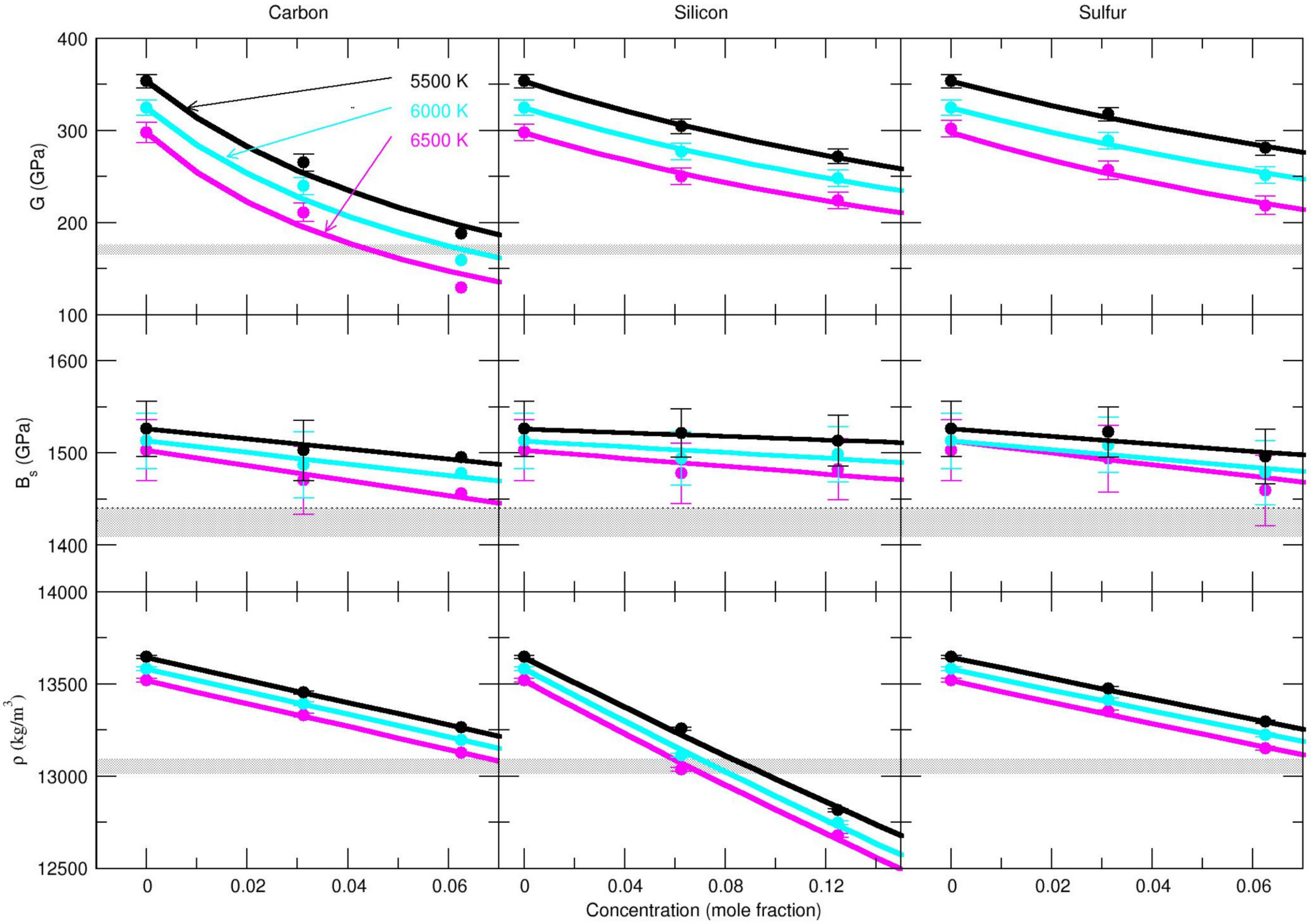

Fig. 3. Fitting the ideal mixing solid solution model. Dots show the calculated G, B_s, and ρ of the *hcp*-Fe alloyed with Si, C, and S, respectively, at 360 GPa. Solid lines show the fitted curves from the solid solution model. Shaded regions indicate the PREM data.

Table 1
The elastic properties of ternary alloys predicted by the solid solution (SS) model in comparison with the calculated data by AIMD.

	Method	ρ (g/cm^3)	B_s (GPa)	G (GPa)	V_s (km/s)	V_p (km/s)
$Fe_{60}Si_3C_1$	AIMD	13.069	1475	223	4.13	11.65
	SS Model	12.951	1481	212	4.05	11.67
$Fe_{60}Si_2C_2$	AIMD	13.119	1481	177	3.67	11.44
	SS Model	13.098	1472	184	3.74	11.45
$Fe_{60}S_3Si_1$	AIMD	13.090	1462	222	4.12	11.59
	SS Model	13.137	1471	228	4.17	11.62
$Fe_{60}Si_2S_2$	AIMD	13.068	1482	233	4.22	11.71
	SS Model	13.113	1478	236	4.24	11.69

vidual elastic constants. This sort of simple model works very well for many systems and has been widely used to calculate the elastic properties of realistic mantle solid solutions (e.g. Chantel, 2014; Pamato et al., 2016).

The partial molar volumes, B_s and G of the Fe, S, Si, and C components were obtained by fitting the ideal solution model to the *ab initio* results for the binary systems. The data are listed in Table S4 and Fig. 3 shows the result of the fitting for the binaries. As can be seen, the calculated elastic properties of binary alloys are well reproduced by this ideal solid solution model. The standard deviations of G, B_s, and ρ are shown in Table S5.

As a further test of the model, we compared the elastic constants and density of the model with the results from the ternary systems obtained directly from the *ab initio* simulations. These results were not used in the fitting and so are a good test of the model. The results are given in Table 1.

3.4. Implication for the inner core

The elastic properties of any *hcp*-Fe–Si–C–S alloy can then be predicted using the mixing model. We, therefore, searched the *hcp*-Fe–Si–C–S system using this solid solution model and located all the possible solutions which predict the density, V_s and V_p of the inner core to within error. The tolerance of errors for the density and sound velocities were a sum of the calculation errors, fitting deviations, and PREM uncertainties. The PREM uncertainties were derived by comparing different Earth's models (IRIS, DMC, 2011).

In addition to the *hcp*-$Fe_{60}Si_2C_2$ solution we found from the *ab initio* simulations directly, many other ternary and quaternary alloys are also able to satisfy both the density and sound velocity constraints within the tolerance. These are shown in Figs. 4A to C. However, many of these solutions may fail if the melting temperature is considered. As can be seen in Figs. 4D to F, the number of allowed solutions is strongly reduced if we remove compositions which are above the melting temperature.

A striking feature of the allowed compositions is that C exists in all the possible candidates and that there are no solutions con-

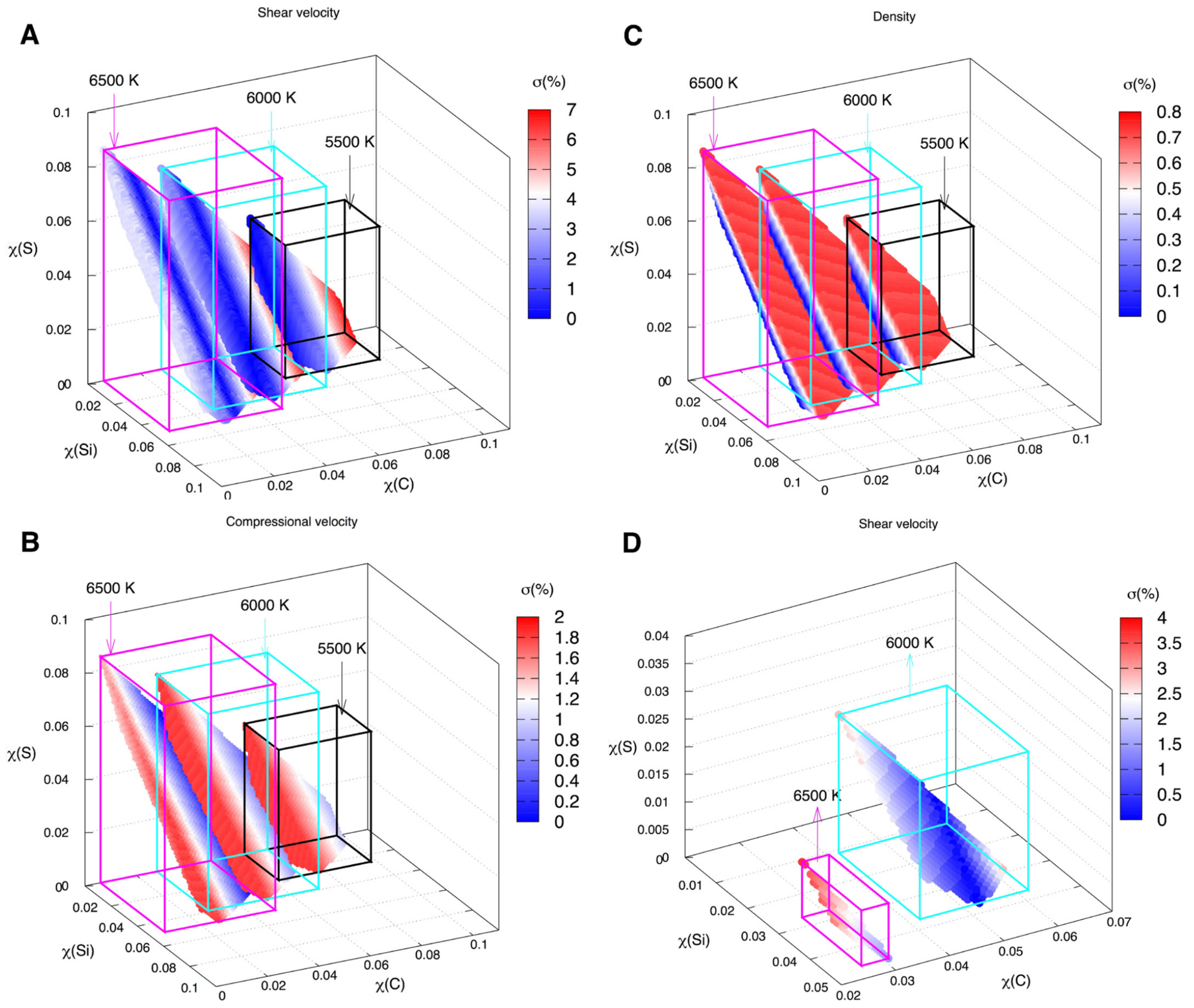

Fig. 4. (**A** to **C**) show the deviations σ(%) of V_s, V_p and ρ from PREM model for the possible candidate compositions at 5500 K, 6000 K, and 6500 K, respectively, from the solid solution model. The number of candidates was further reduced by applying the melting temperature constraint, and the survived compositions are shown in (**D** to **F**). The rectangular boxes in figures indicate the compositional ranges of the candidates at 5500 K, 6000 K, and 6500 K, respectively.

taining only S and Si. This is in agreement with the recent study on iron compounds that no binary Fe–Si or Fe–S compounds can simultaneously match the inner-core density and sound velocities (Bazhanova et al., 2017). The molar fraction of C in the suitable alloy compositions is at least 0.7% at 6500 K, 3% at 6000 K, and 6.3% at 5500 K, respectively.

4. Conclusions

We investigated the elastic properties of the multicomponent *hcp*-Fe alloys under inner core conditions using *ab initio* molecular dynamics calculations. It is found that no binary system can be the candidate of inner core composition. A ternary *hcp*-$Fe_{30}Si_1C_1$ alloy was found to satisfy both the density and sound velocity constraints. Based on an ideal mixing solid solution model, a number of other ternary and quaternary alloys are also able to satisfy the density and velocity constraints; however, in all cases, carbon is an essential component. We have not as yet tested hydrogen or small amounts of oxygen, which may also mix to provide suitable solutions. Our calculations also say nothing about the relative thermodynamic stability of these phases. Nevertheless, this work shows that a mixture of light elements can explain the properties of the inner core, without resorting to anelastic or premelting phenomena.

Acknowledgements

This work was supported by NERC grant NE/M015181/1. Calculations were performed using the ARCHER supercomputer facility. Y.L. carried out the simulations and analyses. L.V. and J.B. supervised the project and contributed to the solid solution model. All authors contributed to writing the paper. Y.L. thanks Martha Pamato, Benjamí Martorell, and Ian G. Wood for fruitful discussions. The data generated during and/or analyzed during the current study are available on reasonable request. Correspondence and requests for materials should be addressed to yunguo.li@ucl.ac.uk.

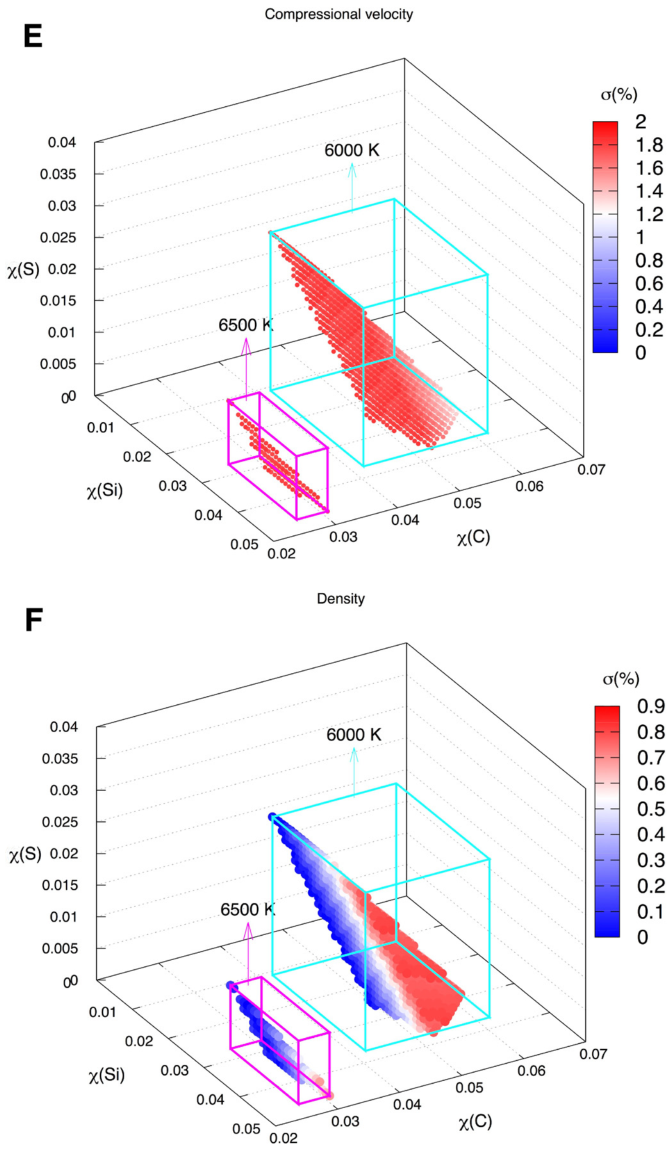

Fig. 4. (*continued*)

Appendix A. Supplementary material

Supplementary material related to this article can be found online at https://doi.org/10.1016/j.epsl.2018.04.013.

References

Alfè, D., 2009. Temperature of the inner-core boundary of the Earth: melting of iron at high pressure from first-principles coexistence simulations. Phys. Rev. B 79, 060101.

Alfè, D., Gillan, M.J., Price, G.D., 2000. Constraints on the composition of the Earth's core from *ab initio* calculations. Nature 405, 172–175.

Alfè, D., Gillan, M.J., Price, G.D., 2002. Composition and temperature of the Earth's core constrained by combining *ab initio* calculations and seismic data. Earth Planet. Sci. Lett. 195, 91–98.

Antonangeli, D., Siebert, J., Badro, J., Farber, D.L., Fiquet, G., Morard, G., Ryerson, F.J., 2010. Composition of the Earth's inner core from high-pressure sound velocity measurements in Fe–Ni–Si alloys. Earth Planet. Sci. Lett. 295, 292–296.

Badro, J., Brodholt, J.P., Piet, H., Siebert, J., Ryerson, F.J., 2015. Core formation and core composition from coupled geochemical and geophysical constraints. Proc. Natl. Acad. Sci. 112, 12310–12314.

Badro, J., Côté, A.S., Brodholt, J.P., 2014. A seismologically consistent compositional model of Earth's core. Proc. Natl. Acad. Sci. 111, 7542–7545.

Bazhanova, Z.G., Oganov, A.R., Gianola, O., 2012. Fe–C and Fe–H systems at pressures of the Earth's inner core. Phys. Usp. 55, 489–497.

Bazhanova, Z.G., Roizen, V.V., Oganov, A.R., 2017. High-pressure behavior of the Fe–S system and composition of the Earth's inner core. arXiv:1703.01214.

Belonoshko, A.B., Skorodumova, N.V., Davis, S., Osiptsov, A.N., Rosengren, A., Johansson, B., 2007. Origin of the low rigidity of the Earth's inner core. Science 316, 1603–1605.

Brodholt, J., Badro, J., 2017. Composition of the low seismic velocity E' layer at the top of Earth's core. Geophys. Res. Lett. 44, 8303–8310.

Caracas, R., 2015. The influence of hydrogen on the seismic properties of solid iron. Geophys. Res. Lett. 42, 3780–3785.

Chantel, J., 2014. Measurement of Elastic Properties of Silicates at Realistic Mantle Pressures. Fakultät für Biologie, Chemie und Geowissenschaften Universität Bayreuth, Bayreuth.

Chen, B., Li, Z., Zhang, D., Liu, J., Hu, M.Y., Zhao, J., Bi, W., Alp, E.E., Xiao, Y., Chow, P., et al., 2014. Hidden carbon in Earth's inner core revealed by shear softening in dense Fe_7C_3. Proc. Natl. Acad. Sci. 111, 17755–17758.

Crosson, R.S., Lin, J.-W., 1971. Voigt and Reuss prediction of anisotropic elasticity of dunite. J. Geophys. Res., Solid Earth 76, 570–578.

DMC, 2011. Data Services Products: EMC, a Repository of Earth Models.

Dziewonski, A.M., Anderson, D.L., 1981. Preliminary reference Earth model. Phys. Earth Planet. Inter. 25, 297–356.

Flyvbjerg, H., Petersen, H.G., 1989. Error estimates on averages of correlated data. J. Chem. Phys. 91, 461–466.

Hernández, E., 2001. Metric-tensor flexible-cell algorithm for isothermal–isobaric molecular dynamics simulations. J. Chem. Phys. 115, 10282–10290.

Hillgren, V.J., Gessmann, C.K., Li, J., 2000. An experimental perspective on the light element in Earth's core. In: Origin of the Earth and Moon, pp. 245–263.

Hirose, K., Morard, G., Sinmyo, R., Umemoto, K., Hernlund, J., Helffrich, G., Labrosse, S., 2017. Crystallization of silicon dioxide and compositional evolution of the Earth's core. Nature 543, 99–102.

Kamada, S., Ohtani, E., Terasaki, H., Sakai, T., Miyahara, M., Ohishi, Y., Hirao, N., 2012. Melting relationships in the $Fe–Fe_3S$ system up to the outer core conditions. Earth Planet. Sci. Lett. 359, 26–33.

Karki, B.B., Stixrude, L., Wentzcovitch, R.M., 2001. High-pressure elastic properties of major materials of Earth's mantle from first principles. Rev. Geophys. 39, 507–534.

Kresse, G., Furthmüller, J., 1996. Efficiency of *ab-initio* total energy calculations for metals and semiconductors using a plane-wave basis set. Comput. Mater. Sci. 6, 15–50.

Kresse, G., Joubert, D., 1999. From ultrasoft pseudopotentials to the projector augmented-wave method. Phys. Rev. B 59, 1758.

Li, J., Fei, Y., Mao, H., Hirose, K., Shieh, S., 2001. Sulfur in the Earth's inner core. Earth Planet. Sci. Lett. 193, 509–514.

Li, Y., Vočadlo, L., Brodholt, J., Wood, I., 2016. Thermoelasticity of Fe_7C_3 under inner core conditions. J. Geophys. Res., Solid Earth 121, 5828–5837.

Litasov, K., Shatskiy, A., 2016. Composition of the Earth's core: a review. Russ. Geol. Geophys. 57, 22–46.

Martorell, B., Brodholt, J., Wood, I.G., Vočadlo, L., 2013a. The effect of nickel on the properties of iron at the conditions of Earth's inner core: ab initio calculations of seismic wave velocities of Fe–Ni alloys. Earth Planet. Sci. Lett. 365, 143–151.

Martorell, B., Vočadlo, L., Brodholt, J., Wood, I.G., 2013b. Strong premelting effect in the elastic properties of *hcp*-Fe under inner-core conditions. Science 342, 466–468.

Martorell, B., Wood, I.G., Brodholt, J., Vočadlo, L., 2016. The elastic properties of hcp-$Fe_{1-x}Si_x$ at Earth's inner-core conditions. Earth Planet. Sci. Lett. 451, 89–96.

Moakher, M., Norris, A.N., 2006. The closest elastic tensor of arbitrary symmetry to an elasticity tensor of lower symmetry. J. Elast. 85, 215–263.

Morard, G., Andrault, D., Antonangeli, D., Bouchet, J., 2014. Properties of iron alloys under the Earth's core conditions. C. R. Géosci. 346, 130–139.

Nadal, M.-H., Le Poac, P., 2003. Continuous model for the shear modulus as a function of pressure and temperature up to the melting point: analysis and ultrasonic validation. J. Appl. Phys. 93, 2472–2480.

Oganov, A.R., Brodholt, J.P., Price, G.D., 2001. The elastic constants of $MgSiO_3$ perovskite at pressures and temperatures of the Earth's mantle. Nature 411, 934–937.

Pamato, M.G., Kurnosov, A., Boffa Ballaran, T., Frost, D.J., Ziberna, L., Giannini, M., Speziale, S., Tkachev, S.N., Zhuravlev, K.K., Prakapenka, V.B., 2016. Single crystal elasticity of majoritic garnets: stagnant slabs and thermal anomalies at the base of the transition zone. Earth Planet. Sci. Lett. 451, 114–124.

Perdew, J.P., Wang, Y., 1992. Accurate and simple analytic representation of the electron-gas correlation energy. Phys. Rev. B 45, 13244–13249.

Prescher, C., Dubrovinsky, L., Bykova, E., Kupenko, I., Glazyrin, K., Kantor, A., McCammon, C., Mookherjee, M., Nakajima, Y., Miyajima, N., et al., 2015. High Poisson's ratio of Earth's inner core explained by carbon alloying. Nat. Geosci. 8, 220–223.

Sakamaki, T., Ohtani, E., Fukui, H., Kamada, S., Takahashi, S., Sakairi, T., Takahata, A., Sakai, T., Tsutsui, S., Ishikawa, D., Shiraishi, R., Seto, Y., Tsuchiya, T., Baron, A.Q.R., 2016. Constraints on Earth's inner core composition inferred from measurements of the sound velocity of hcp-iron in extreme conditions. Sci. Adv. 2.

Simmons, G., Wang, H., et al., 1971. Single Crystal Elastic Constants and Calculated Aggregate Properties: a Handbook. MIT Press, Mass.

Tagawa, S., Ohta, K., Hirose, K., Kato, C., Ohishi, Y., 2016. Compression of Fe–Si–H alloys to core pressures. Geophys. Res. Lett. 43, 3686–3692.

Umemoto, K., Hirose, K., 2015. Liquid iron–hydrogen alloys at outer core conditions by first-principles calculations. Geophys. Res. Lett. 42, 7513–7520.

van de Walle, A., Tiwary, P., de Jong, M., Olmsted, D.L., Asta, M., Dick, A., Shin, D., Wang, Y., Chen, L.Q., Liu, Z.K., 2013. Efficient stochastic generation of special quasirandom structures. Calphad 42, 13–18.

Vočadlo, L., 2007. Ab initio calculations of the elasticity of iron and iron alloys at inner core conditions: evidence for a partially molten inner core? Earth Planet. Sci. Lett. 254, 227–232.

Vočadlo, L., Alfè, D., Gillan, M.J., Price, G.D., 2003. The properties of iron under core conditions from first principles calculations. Phys. Earth Planet. Inter. 140, 101–125.

Wallace, D.C., 1998. Thermodynamics of Crystals. Courier Corporation.

Wood, B.J., Li, J., Shahar, A., 2013. Carbon in the core: its influence on the properties of core and mantle. Rev. Mineral. Geochem. 75, 231–250.

Zhang, Y., Yin, Q.-Z., 2012. Carbon and other light element contents in the Earth's core based on first-principles molecular dynamics. Proc. Natl. Acad. Sci. 109, 19579–19583.

Zunger, A., Wei, S.-H., Ferreira, L., Bernard, J.E., 1990. Special quasirandom structures. Phys. Rev. Lett. 65, 353.